Research Square

Preprints are preliminary reports that have not undergone peer review.
They should not be considered conclusive, used to inform clinical practice,
or referenced by the media as validated information.

Determining Dielectric Constant and Loss Factor of Concrete Panels from GPR A-scan Curves – Theory, Numerical Simulation, and Experimental Validation

Tzuyang Yu

Tzuyang_Yu@uml.edu

University of Massachusetts Lowell

Maryam Abazarsa

University of Massachusetts Lowell

Research Article

Keywords: Electromagnetic sensing, GPR, dielectric constant, loss factor, concrete, FDTD, CWT, FFT

Posted Date: June 18th, 2026

DOI: https://doi.org/10.21203/rs.3.rs-9838617/v1

License: This work is licensed under a Creative Commons Attribution 4.0 International License.
Read Full License

Additional Declarations: No competing interests reported.

Determining Dielectric Constant and Loss Factor of Concrete Panels from GPR A-scan Curves – Theory, Numerical Simulation, and Experimental Validation

Tzuyang Yu[*1], Maryam Abazarsa[2]

[1]Professor, Tzuyang_Yu@uml.edu

[2]Doctoral Candidate, Maryam_Abazarsa@student.uml.edu

Department of Civil and Environmental Engineering

University of Massachusetts Lowell

Lowell, Massachusetts 01854, USA

[*]Corresponding Author: Email: Tzuyang_Yu@uml.edu

ABSTRACT

Electromagnetic (EM) sensors such as ground penetrating radar (GPR) have been widely used in the inspection of concrete structures (e.g., buildings, bridges) for condition assessment and health monitoring. To fully understand the GPR result, the EM property (dielectric constant and loss factor) of concrete should be known for account for changing phase velocity and amplitude attenuation of GPR signals inside concrete. The objective of this paper is to present an approach to extract both the dielectric constant and the loss factor of concrete panel specimens from A-scan curves. An analytical derivation is first provided as the theoretical basis of our approach. Numerical simulations using the finite different time domain (FDTD) method are applied to generate GPR A-scan curves of homogeneous concrete panel models with a varying dielectric constant in the range of 5 to 25 at a constant electrical conductivity 0.1 S/m. A 1.6GHz Ricker wavelet function signal was used in generating all simulated A-scan curves containing two wave

packets (the front reflection and the back reflection of a concrete panel model). Continuous wavelet transform (CWT) was applied to determine the center of two wave packets in the time domain. Spectral amplitude of A-scan curves was used to quantify signal attenuation from the front reflection to the back reflection. A modification factor was proposed to account for geometric scattering effects in the estimation of loss factor. Proposed approach was applied to an experimentally measured 1.6GHz GPR A-scan curve and verified by the coaxial probe measurement (0.4~2.9 GHz). From our result, it is found that our estimated dielectric constant and loss factor are bounded by Debye's model and coaxial probe measurement. Our predicted dielectric constant is very close to the probe measurement, while our predicted loss factor is very close to the theoretical value of Debye's model.

Keywords: Electromagnetic sensing, GPR, dielectric constant, loss factor, concrete, FDTD; CWT, FFT

Introduction

Nondestructive testing/evaluation (NDT/E) of concrete structures (e.g., bridges, buildings, roadways, tunnels, airports, nuclear power plants) provides useful information for condition assessment to achieve effective repair in modern asset management. Among existing NDT/E techniques, electromagnetic (EM) and radar methods, such as ground penetrating radar (GPR) and synthetic aperture radar (SAR), offer unique capabilities for in-situ subsurface inspection of concrete structures. Compared to SAR, GPR is a commercially mature, widely used technology in many engineering and science disciplines such as civil engineering, mechanical engineering, and geophysics. GPR produces four different data formats, including 1D A-scan curve, 2D B-scan image, 3D C-scan volume, and 2D D-scan image. The ability of EM waves to travel inside porous

dielectrics like Portland cement concrete enables imaging radar sensors to reconstruct the subsurface composition of concrete structures. This ability is based on the finite EM property of concrete, namely the complex electric permittivity (farads/meter or F/m) and the complex magnetic permeability (henrys/meter or H/m). Since most concretes are generally considered non-magnetic, it is their complex electric permittivity that fundamentally affects the performance of imaging radar sensors on concrete structures.

In engineering applications, complex electric permittivity is usually normalized into a dimensionless, complex relative electric permittivity whose real part is called dielectric constant and imaginary part called loss factor. Dielectric constant is related to concrete's ability to store EM energy (change of EM wave velocity), while loss factor is related to concrete's ability to dissipate EM energy (change of EM wave amplitude). Dielectric constant of concrete affects ranging accuracy in the radar images of concrete. Loss factor of concrete affects the amplitude and phase of radar signals in concrete. These two parameters are also called the dielectric properties. Both parameters change the formation of radar images, as well as how we interpret radar images of concrete structures.

Dielectric properties of concrete alone can also be used to indicate the condition of concrete. Dielectric constant of concrete is related to the density and porosity of concrete, which can be used to indicate the age and design of fresh concrete, presence of cracking, pore size distribution, and moisture content of concrete structures. Dielectric constant of fresh concrete decreases with the increase of frequency and curing time, due to the loss of moisture content in cement hydration [1,2]. It increases with the increase of chloride content at low frequencies (~50MHz) and becomes negligible at high frequencies (~1GHz) [3]. The effect of cement hydration on moisture content

66 inside concrete is most prominent for the concretes under the age of 28 days [3]. Dielectric constant
67 increases with the increases of concrete density when high-density aggregates are used [4]. Lower
68 water-to-cement (w/c) ratios lead to higher dielectric constants of fresh concrete, which can be
69 used to indicate the compressive strength of concrete [1]. Dielectric constant of old concrete also
70 decreases with the increase of frequency but to a less extent when compared to fresh concrete.
71 Dielectric constant of old concrete decreases initially with the increase of temperature (up to ~400
72 °C) and increases again (above 500 °C) due to solid-phase transformations [5].

73 Loss factor of fresh concrete is related to the curing of concrete, the presence of moisture and
74 chloride contents, which can also be used to indicate concrete cracking and steel rebar corrosion
75 of concrete structures. Loss factor of fresh concrete decreases with the frequency and curing time,
76 due to the loss of moisture content [1,2]. Loss factor of old concrete increases with the decrease of
77 the w/c ratio and the increase of density [5]. Loss factor of fresh concrete increases when cured by
78 moisture rather than air [4].

79 Measurement of dielectric properties is commonly performed over a range of frequencies in
80 dielectric spectroscopy[6,7] as a function of frequency or in dielectric time domain reflectometry
81 (TDR) [1,2,4,8,9] or dielectric time domain transmissometry (TDT) [10]. Measurement techniques
82 include the free-space method [2,4,6,7,10], capacitor method, resonant cavity method, coaxial
83 probe method [3,9], waveguide method [6,11], and GPR method [8,12–17]. Klysz *et al.* (2004)
84 [18].] applied the spectral analysis of radar surface waves (SARSW) to their 600M and 1.3GHz
85 GPR A-scan curves from one concrete panel to calculate the frequency-dependent phase velocity
86 of GPR signals in concrete. Later, Klysz *et al.* (2008) [8] used a 1.5GHz GPR system to collect
87 A-scan curves from nine concrete panels (60×60×12 cm^3) and the finite difference time domain

(FDTD) method to simulate measured A-scan curves. Their approach of calculating dielectric constant was from the phase velocity of GPR signals in concrete, which was determined from the time difference of arrival (TDOA). They used a low electrical conductivity value of 0.0001 S/m from literature in their FDTD simulation [19]. While their estimated dielectric constant and electrical conductivity values of concrete from A-scan curve matching/adjustment, no empirical equations were provided from their result. There was also no calculation on the loss factor of concrete in their result. Lai *et al.* (2009) [14] used the GPR A-scan curves of lightweight aggregate concrete (LWAC) and normal aggregate concrete (NAC) panel/slab specimens (200×200×150 mm^3) to calculate dielectric constant of LWAC and NAC at different ages (1~90 days), using a 1GHz GPR system. They used the TDOA in A-scan curves to calculate the phase velocity of GPR signals, as a function of the dielectric constant of concrete. No calculation of the loss factor of concrete in their result was reported. Chen *et al.* (2012) [13] also used the GPR A-scan curves of cement mortar and concrete panel specimens (300×250×100 mm^3) enclosed by a backing steel plate inside a polymethylmethacrylate container to study the correlation between dielectric constant and moisture content, temperature, fly ash content, and slag content. They used a 1.5GHz GPR system and showed that the dielectric constant of concrete increases with the increase of moisture content, while decreasing with the increase of temperature. They also used the TDOA to calculate the phase velocity of GPR signals to calculate the dielectric constant of concrete. Wong and Lai (2022) [12] applied the GPRMax to generate A-scan curves of concrete panel models in four different scenarios (dry, half-saturated, saturated, and chloride-contaminated). They used a 2D concrete model and five frequencies (0.4, 0.5, 0.6, 0.7, and 1.3 GHz) in their simulation. The dielectric constant of their concrete models was estimated by using the complex refractive index model. They applied Debye's model to show the theoretical values of dielectric constant and loss

111 factor. In their simulation result, they used the TDOA in A-scan curves to calculate the dielectric
112 constant of concrete models. He *et al.* (2023) [15] conducted a field study to measure the dielectric
113 constant and the electrical resistivity (inverse of electrical conductivity) of two concrete slabs
114 (1,830×2,440×200 mm^3) by using GPR A-scan curves. Similar to Chen *et al.* (2012) [13], they
115 also used two steel sheets at the bottom of concrete slabs to amplify the back reflection. They used
116 a 1.6GHz GPR and two approaches to calculate dielectric constant; the TDOA approach and the
117 first pulse amplitude approach. From their result, they found that the TDOA approach shows a
118 stable decay pattern with specimen age, while the first pulse amplitude approach shows unstable,
119 fluctuating pattern with specimen age. Their finding demonstrated the issue with the time-domain
120 information in A-scan curves, which can affect the accuracy of calculated dielectric constant. He
121 and Lu (2023) [16] used GPR A-scan curves of concrete beam specimens (152×152×559 mm^3) to
122 study the correlation between dielectric constant and specimen age by using 1.6 and 2.6 GHz
123 frequencies. Three different curing conditions (air-cured, water-cured, and compound-cured) and
124 two w/c ratios (0.4 and 0.5) were considered. They used the amplitude ratio of positive peaks in
125 an A-scan curve to quantify EM attenuation of concrete. They also presented the correlation
126 between dielectric constant and EM attenuation, showing a negative linear pattern between
127 dielectric constant and EM attenuation [20]. Hou *et al.* (2025) [17] simulated GPR A-scan curves
128 of concrete models (1,500×1,500×80 and 50 mm^3) by PFC3D and GPRMax at 0.8, 1, 1.2, 1.6, and
129 2.0 GHz frequencies to estimate the dielectric constant of concrete. They used a deep learning
130 approach to compute the dielectric constant of concrete from A-scan curves extracted from 300
131 concrete slab models with 1,500 data groups. From our literature review, most GPR methods used
132 the TDOA in A-scan curves to calculate the dielectric constant of concrete. There is no reported
133 approach on the calculation of loss factor of concrete using A-scan curves in the literature.

Determining the dielectric constant of concrete specimens using GPR A-scan curves is feasible but dependent on four major factors: signal wavelength vs. specimen thickness, specimen geometry, material's heterogeneity, and the loss factor of concrete. To calculate accurate TDOA from A-scan curves, destructive interference between the front reflection (or direct coupling) and the back reflection wave packets should be avoided if possible, suggesting a minimum specimen thickness greater than the chosen wavelength. Corner scattering from the finite size/shape effect of concrete specimens should also be avoided. Multiple reflections among the heterogeneous inclusions in concrete can also distort TDOA measurements. Attenuation of signal amplitude due to the dielectric loss of concrete can further make TDOA measurements of the back reflection difficult (diminishing back reflection amplitude), resulting in the calculation errors of dielectric constant of concrete.

On the other hand, determining the loss factor of concrete specimens using GPR A-scan curves is a very challenging task, especially when using TDOA. This is because, attenuation of GPR signals (or EM waves) inside concrete is caused by dielectric loss and conductivity loss. Both contribute differently to amplitude attenuation and phase shift, depending on measurement frequency and moisture content of concrete. Furthermore, when measuring amplitude attenuation in A-scan curves, the use of finite wave packets (or impulses) makes both the positive and the negative amplitudes in A-scan curves very sensitive to phase shift and destructive interference. This sensitivity also attributes to the errors in the calculation of loss factor of concrete.

The objective of this paper is to propose a physical approach to calculate both dielectric constant and loss factor of concrete panels by using GPR A-scan curves. First, a modified TDOA approach for calculating dielectric constant is proposed by using continuous wavelet transform (CWT).

TDOA is calculated between two numbers of peak amounts (front and back reflections) in the time domain, rather than directly using either positive or negative peak amplitudes in an A-scan curve. Derivation from the complex wavenumber to the amplitude attenuation in A-scan curves as a function of dielectric loss factor and electrical conductivity is provided. An empirical function M responsible for the moisture dependence of dielectric constant (since moisture content can affect dielectric constant, loss factor, and static electrical conductivity) is proposed. To test our approach, synthetic GPR A-scan curves are generated from six concrete panel models by using GPRMax with a 1.6GHz ricker wavelet signal. Model parameters of concrete are taken from reported experimental data in the literature to ensure the veracity of our simulation. To validate our approach, a 1.6GHz GPR system was used to collect experimental A-scan curve from a laboratory concrete panel specimen.

2. Research Approach

2.1. Wave Propagation Time and Dielectric Constant

From the Helmholtz wave equation of EM waves, the phase velocity v_p of EM waves in free space (or air) is

$$v_p = \frac{1}{\sqrt{\varepsilon_0 \mu_0}} \quad (1)$$

where $\varepsilon_0 = 8.854 \times 10^{-12}$ farads/m (F/m) is the electric permittivity of air is and $\mu_0 = 4\pi \times 10^{-7}$ henrys/m (H/m) the magnetic permeability of air. $v_p \cong 2.998 \times 10^8$ (m/s) is also denoted by c. The dispersion relation provides

$$k^2 = \omega^2 \varepsilon_0 \mu_0 \quad (2)$$

where k is the wavenumber or spatial frequency (in 1/m) and ω the angular frequency (rad/s). Equivalently,

$$k = \frac{\omega}{v_p} \tag{3}$$

Or

$$v_p = \frac{\omega}{k} \tag{4}$$

In the presence of electrical conductivity (lossy dielectrics), wavenumber k becomes complex and the dielectric is considered lossy. We should use the real part of k for lossy dielectrics in Eq.(4). The electrical property of lossy dielectrics is defined by the complex electric permittivity ε^* (F/m) written by

$$\varepsilon^* = \varepsilon' - j\varepsilon'' \tag{5}$$

where ε' is the real part of ε^* and ε'' the imaginary part of ε^*. $j = \sqrt{-1}$ is the imaginary number. In engineering, it is customary to normalize it by

$$\varepsilon_r^* = \frac{\varepsilon^*}{\varepsilon_0} = \varepsilon_r' - j\varepsilon_r'' \tag{6}$$

where ε_r^* is the dimensionless, relative complex electric permittivity. ε_r' is known as the dielectric constant and ε_r'' the loss factor of a dielectric. Similarly, the magnetic property of lossy dielectrics is defined by the complex magnetic permeability μ^* (H/m) written by

$$\mu^* = \mu' - j\mu'' \tag{7}$$

where μ' is the real part of μ^* and μ'' the imaginary part of μ^*. It is also costumery normalize by

$$\mu_r^* = \frac{\mu^*}{\mu_0} = \mu_r' - j\mu_r'' \tag{8}$$

where μ_r^* is the dimensionless, relative complex magnetic permeability. From [Kong (2000)], the phase velocity inside a lossy dielectric is

$$v_p = \frac{\omega}{k_R} = \frac{1}{\sqrt{\mu'\varepsilon'}}\left[\frac{1}{2}\left(\sqrt{1+\left(\frac{\sigma_{DC}}{\omega\varepsilon'}\right)^2}\right)\right]^{-1/2} \quad (9)$$

where σ_{DC} is the DC (direct current) electrical conductivity (S/m). Since

$$\mu' = \mu_r'\mu_0 \quad (10a)$$

$$\varepsilon' = \varepsilon_r'\varepsilon_0 \quad (10a)$$

we also have

$$v_p = \frac{c}{\sqrt{\mu_r'\varepsilon_r'}}\left[\frac{1}{2}\left(\sqrt{1+\left(\frac{\sigma_{DC}}{\omega\varepsilon'}\right)^2}\right)\right]^{-1/2} \quad (11)$$

When a dielectric is low-loss or at high frequencies, $\frac{\sigma_{DC}}{\omega\varepsilon'} \approx 0$ and

$$v_p \approx \frac{c}{\sqrt{\mu_r'\varepsilon_r'}} \quad (12)$$

Since most construction materials such as concrete, wood, and asphalt are non-magnetic, $\mu_r' = 1$ and $\mu_r'' = 0$. The phase velocity of EM waves can be approximated by

$$v_p \approx \frac{c}{\sqrt{\varepsilon_r'}} \quad (13)$$

If we can measure the propagation time t at a known propagation distance s within a dielectric specimen, we have

$$\frac{c}{\sqrt{\varepsilon_r'}} = \frac{s}{t} \quad (14)$$

such that

$$(\varepsilon_r')_A = \left(\frac{ct}{s}\right)^2 \tag{15}$$

which is the time of arrival (TOA) approach for estimating the dielectric constant of a material specimen and similar to the TDOA approach [10]. Eq. (15) will be used to estimate the effective dielectric constant from concrete models in our synthetic A-scan curves. For reflection-only measurements on a panel specimen with a thickness *d*, the TOA represents the time traveling from the front interface to the back interface then back to the front interface. As illustrated in Fig. 1, time instants t_1 and t_2 are TOA by using t_0 as a reference time zero. The difference between t_1 and t_2 is TDOA (or t) that is related to the thickness of a concrete panel specimen.

$$t = t_2 - t_1 = \frac{2d\sqrt{(\varepsilon_r')_A}}{c} \tag{16}$$

where d is the thickness of a concrete panel.

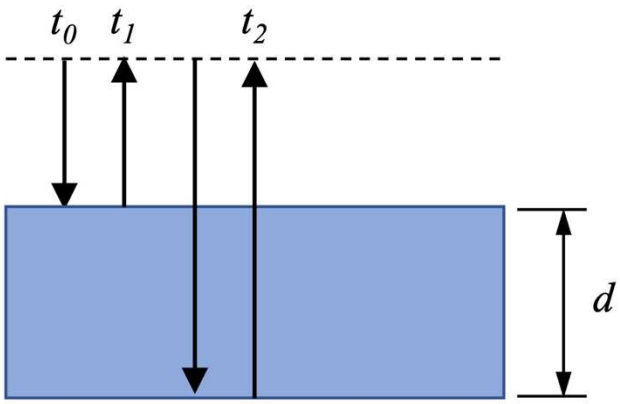


Fig. 1. Reflection-only measurement on a panel specimen.

2.2. Wave Attenuation and Loss Factor

To determine the loss factor of a material specimen from the time domain, we use the attenuation of GPR signals. The complex wavenumber k^* is defined by

$$k^* = \omega\sqrt{\varepsilon^*\mu^*} = \omega\sqrt{(\varepsilon' - j\varepsilon'')(\mu' - j\mu'')}$$

$$= \omega\sqrt{(\varepsilon'\mu' - \varepsilon''\mu'') - j(\varepsilon'\mu'' + \varepsilon''\mu')} \quad (17)$$

For non-magnetic dielectrics like concrete, $\mu' = \mu_0$ and $\mu'' = 0$.

$$k^* = \omega\sqrt{\varepsilon'\mu' - j\varepsilon''\mu'} = \omega\sqrt{\varepsilon'\mu'}\sqrt{1 - j\left(\frac{\varepsilon''}{\varepsilon'}\right)} \quad (18)$$

With $c = \frac{1}{\sqrt{\varepsilon_0\mu_0}}$ and Eqs. (10a) and (10b), k^* becomes

$$k^* = \frac{\omega\sqrt{\varepsilon_r'}}{c}\sqrt{1 - j\left(\frac{\varepsilon''}{\varepsilon'}\right)} \quad (19)$$

since $\mu_r' = 1$ when $\mu' = \mu_0$. By applying binomial expansion, the square root can be approximated by

$$\sqrt{1 - j\left(\frac{\varepsilon''}{\varepsilon'}\right)} \approx 1 - j\left(\frac{\varepsilon''}{2\varepsilon'}\right) + \frac{1}{2}\left(\frac{\varepsilon''}{2\varepsilon'}\right)^2 \quad (20)$$

such that

$$k^* \approx \frac{\omega\sqrt{\varepsilon_r'}}{c}\left[1 - j\left(\frac{\varepsilon''}{2\varepsilon'}\right) + \frac{1}{2}\left(\frac{\varepsilon''}{2\varepsilon'}\right)^2\right] = \left[\frac{\omega\sqrt{\varepsilon_r'}\left(8\varepsilon'^2 + \varepsilon''^2\right)}{8c\varepsilon'^2}\right] - j\left(\frac{\omega\varepsilon''\sqrt{\varepsilon_r'}}{2c\varepsilon'^2}\right) = \alpha - j\beta \quad (21)$$

where α is the attenuation factor and β the phase factor [21,22]. From Lambert's law [23] attenuation of EM wave intensity can be modeled by

$$I = I_0\exp(-\alpha x) \quad (22)$$

in which the attenuation factor can be written by

$$\alpha = \frac{1}{x}\ln\left(\frac{I_0}{I}\right) \tag{23}$$

where I_0 is the initial intensity and I the attenuated intensity at distance x (specimen thickness). By relating Eqs. (21) and (23), we have

$$\frac{1}{x}\ln\left(\frac{I_0}{I}\right) = \frac{\omega\sqrt{\varepsilon_r'\left(8\varepsilon'^2+\varepsilon''^2\right)}}{8c\varepsilon'^2} \tag{24}$$

leading to the theoretical expression of loss factor in terms of intensity attenuation in the following

$$\varepsilon_r'' = \frac{8c\varepsilon_r'^{1.5}}{\omega x}\ln\left(\frac{I_0}{I}\right) - 8\varepsilon_r'^2 \tag{25}$$

Since Lambert's law does not consider other internal wave scattering effects, Eq. (25) needs to be revised by a modification function M. If we use Eq. (15) to determine ε_r', Eq. (25) provides the estimation of ε_r'' from A-scan curves.

$$\left(\varepsilon_{r,\text{eff}}''\right)_A = \frac{8c\left(\varepsilon_r'\right)_A^{1.5}}{\omega x} M \ln\left(\frac{I_0}{I}\right) - 8\left(\varepsilon_r'\right)_A^2 \tag{26}$$

Equivalently,

$$M = \frac{\omega x}{8c\left(\varepsilon_r'\right)_A^{1.5}}\ln\left(\frac{I}{I_0}\right)\left[\left(\varepsilon_{r,\text{eff}}''\right)_A - 8\left(\varepsilon_r'\right)_A^2\right] \tag{27}$$

The value of M represents the combined effect of material composition, specimen geometry, wave scattering and interference since our approach uses the time-domain GPR A-scan curves. With known concrete model parameters ($\varepsilon'_{\text{static}}$, $\varepsilon'_{\text{inf}}$, σ_{dc}, and τ), we can compare the model predicted $\left(\varepsilon_{r,\text{eff}}''\right)_D$ with the A-scan extracted $\left(\varepsilon_{r,\text{eff}}''\right)_A$ to determine the function M. Since the moisture content of concrete can contribute to the increase of its electric conductivity, the loss factor

calculated by Eq.(26) is actually the effective loss factor containing the contribution of electric conductivity.

2.3. Effect of Static Electrical Conductivity

Since Portland cement concrete is manufactured from cement hydration to produce calcium-silica-hydrate (C-S-H) gels/particles as the binder to hold fine and coarse aggregates, the amorphous structure of C-S-H gels is inherently porous. The porosity of concrete provides the space for liquid water molecules (or moisture) to reside inside or on the surface of C-S-H gels, in the form of chemically bound water (or chemical water) or physically bound water (or physical water). The presence of moisture, together with the free ions (e.g., chloride ions Cl^- and hydroxide ions OH^-), increases the electrical conductivity of concrete. To consider the effect of moisture content in concrete on the dielectric constant and loss factor of concrete, Soutsos *et al.* (2001) and Shaari *et al.* (2004) reported their experimental measurements of concrete specimens with different moisture contents in the frequency range of 1MHz to 2 GHz. The relation between loss factor ε_r'' and static electrical conductivity σ_{dc} is defined by an effective loss factor $\left(\varepsilon_{r,\text{eff}}''\right)_D$.

$$\left(\varepsilon_{r,\text{eff}}''\right)_D = \frac{\omega\tau(\varepsilon_\text{s}'-\varepsilon_\infty')}{1+(\omega\tau)^2} + \frac{\sigma_\text{dc}}{\omega\varepsilon_0} = \frac{\sigma_\text{ac}'}{\omega\varepsilon_0} \tag{28}$$

where ε_s' is the static dielectric constant, ε_∞' the infinite dielectric constant, τ the relaxation time (sec.), and σ_dc the static (direct current) electrical conductivity (siemens/m). In Eq. (28), Debye's dispersion (or relaxation) model with a single relaxation time is assumed. Eq. (28) represents the effective loss factor predicted by Debye's model, hence the notation $\left(\varepsilon_{r,\text{eff}}''\right)_D$. The subscript *D* is used to indicate Debye's model. Eq. (28) also leads to

$$\sigma_\text{ac}' = \omega\varepsilon_0\left(\varepsilon_{r,\text{eff}}''\right)_D = \omega(\varepsilon_\text{eff}'')_D \tag{29}$$

Note that $(\varepsilon''_{\text{eff}})_D = \varepsilon_0\left(\varepsilon''_{r,\text{eff}}\right)_D$ is in the unit of farads/m (F/m), while $\left(\varepsilon''_{r,\text{eff}}\right)_D$ is dimensionless. Eq. (29) is also called dielectric conductivity in the literature. [21]

$$\sigma' = \omega\varepsilon'' \tag{30}$$

In practice, the loss factor of concrete can be measured from specimens by using various measurement techniques. In numerical simulation, $\varepsilon'_{\text{static}}$, $\varepsilon'_{\text{inf}}$, σ_{dc}, and τ must be defined as the EM properties of concrete at a given simulation frequency ω. On the other hand, the dielectric constant calculated from Debye's dispersion model is

$$(\varepsilon'_r)_D = \varepsilon'_\infty + \frac{\varepsilon'_s - \varepsilon'_\infty}{1+(\omega\tau)^2} \tag{31}$$

which is denoted by $(\varepsilon'_r)_D$. In this paper, numerical simulations using the finite difference time domain (FDTD) method are conducted to determine the expression of function M with different EM properties of concrete reported in the literature, by comparing $\left(\varepsilon''_{r,\text{eff}}\right)_A$ from A-scan curves with $\left(\varepsilon''_{r,\text{eff}}\right)_D$ from Debye's model.

3. Time-Domain Electrodynamic Simulation

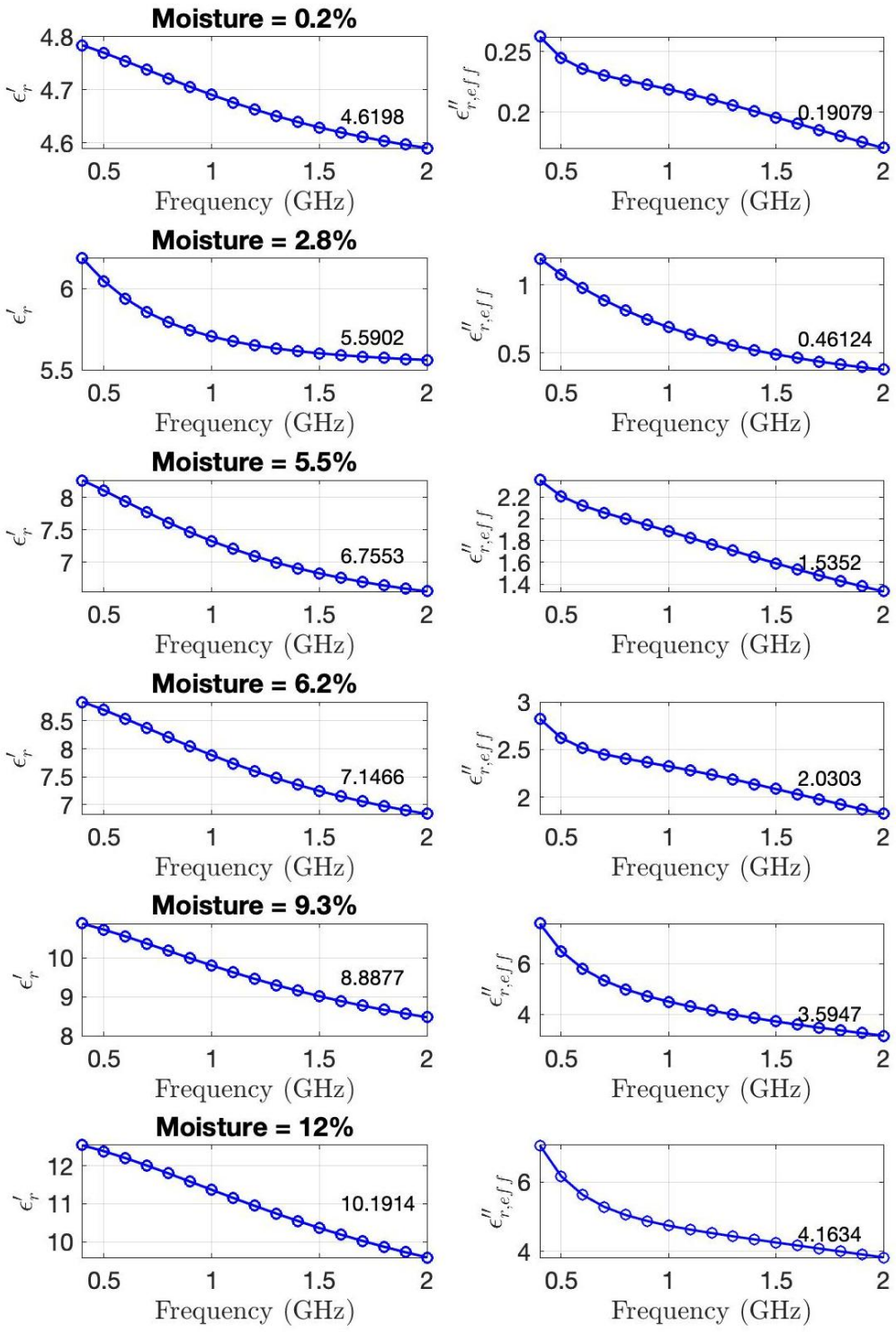
The finite difference time domain (FDTD) method is a mature technique to simulate the time domain response of EM waves (GPR signals) governed by Maxwell's curl equations [24]. It is specifically ideal to simulate the transient response of EM wave propagation, reflection, and scattering of concrete materials and structures [25]. Theoretical basis and formulation about the FDTD method can be found in the literature [24,26–29].

To simulate the attenuation of GPR signals inside concrete, a 2D homogeneous concrete panel model is created using GPRMax [30]. EM properties of the concrete model are taken from

Sandrolini *et al.* (2007) [31], based on the experimental data of concrete specimens with different moisture contents. The experimental data were reported by Soutsos *et al.* (2001) [32] and Shaari *et al.* (2004) [33]. The EM properties of six concrete models (CN1 ~ CN6) used in our FDTD simulations are listed in Table 1. With these model parameters, we can calculate the dielectric constant $(\varepsilon_r')_D$ and the effective loss factor $\left(\varepsilon''_{r,\text{eff}}\right)_D$ of a concrete model from Eqs. (31) and (28), respectively. The experimentally determined $(\varepsilon_r')_D$ and $\left(\varepsilon''_{r,\text{eff}}\right)_D$ are used as the ground truth to compare with the $(\varepsilon_r')_A$ and $\left(\varepsilon''_{r,\text{eff}}\right)_A$ values calculated from A-scan curves. The dispersion curves of six concrete models at different moisture levels are shown in Fig. 2.

Table 1. Electromagnetic properties of concrete models [31]

Model	Moisture content (%)	$\boldsymbol{\varepsilon'_{\text{static}}}$	$\boldsymbol{\varepsilon'_{\text{inf}}}$	$\boldsymbol{\tau}$ (ns)	$\boldsymbol{\sigma_{\text{dc}}}$ (S/m)
CN1	0.2	4.814±0.002	4.507±0.002	0.82±0.01	$6.06\times 10^{-4} \pm 0.06 \times 10^{-4}$
CN2	2.8	6.75±0.03	5.503±0.005	2.28±0.08	$2.03\times 10^{-3} \pm 0.04 \times 10^{-3}$
CN3	5.5	8.63±0.02	6.023±0.009	1.00±0.02	$5.15\times 10^{-3} \pm 0.06 \times 10^{-3}$
CN4	6.2	9.14±0.06	5.93±0.02	0.80±0.03	$6.7\times 10^{-3} \pm 0.3 \times 10^{-3}$
CN5	9.3	11.19±0.05	7.20±0.02	0.73±0.02	$23\times 10^{-3} \pm 2 \times 10^{-3}$
CN6	12.0	12.84±0.03	7.42±0.02	0.611±0.006	$20.6\times 10^{-3} \pm 0.2 \times 10^{-3}$



310

311 **Fig. 2.** Dielectric dispersion curves of six concrete models.

A 2D 0.3048m-by-0.147m (305-by-167 grids) domain was created to accommodate a 2D concrete panel model with a cross section area of 0.3048m-by-0.127m. Eight layers of perfectly matched layer (PML) [34–37] were used as the absorbing boundary condition (ABC) in our FDTD simulation to reduce undesired reflections from four finite boundaries in the rectangular domain. A 1.6GHz ricker function was used as the GPR input signal. CFL stability criterion was adopted to ensure the numerical stability in both the time domain and the space domain [38]. A temporal resolution of Δt = 2.358655 picoseconds and a spatial resolution of Δx = 0.001 meters were used in all simulation cases. Fig. 3 shows the configuration of a concrete panel model used in this research. Locations of the point source (transmitter) and the receiver are also indicated in Fig. 3. In Fig. 3, a simulated GPR system is comprised of a transmitting antenna Tx and a receiving antenna Rx. Fig. 4 shows the 1.6GHz ricker function as the input GPR signal in the time domain and the frequency domain. Fig. 2 also shows the values of the dielectric constant ε_r' and the effective loss factor $\varepsilon_{r,\text{eff}}''$ of six concrete models at 1.6GHz.

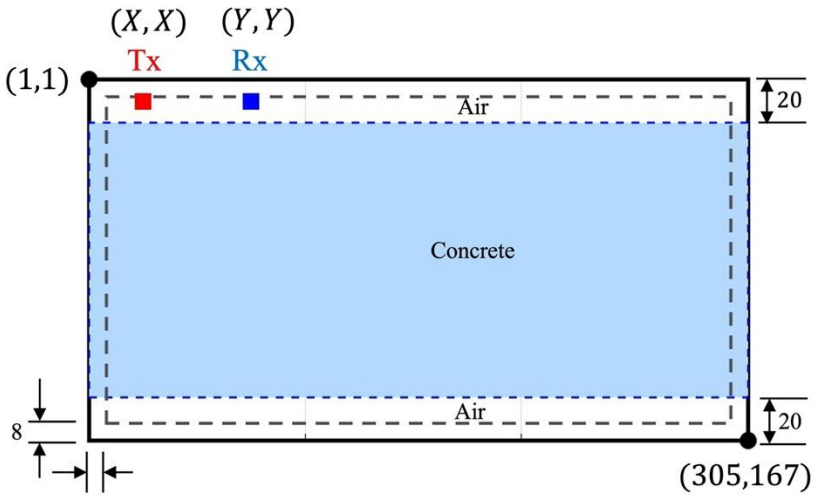
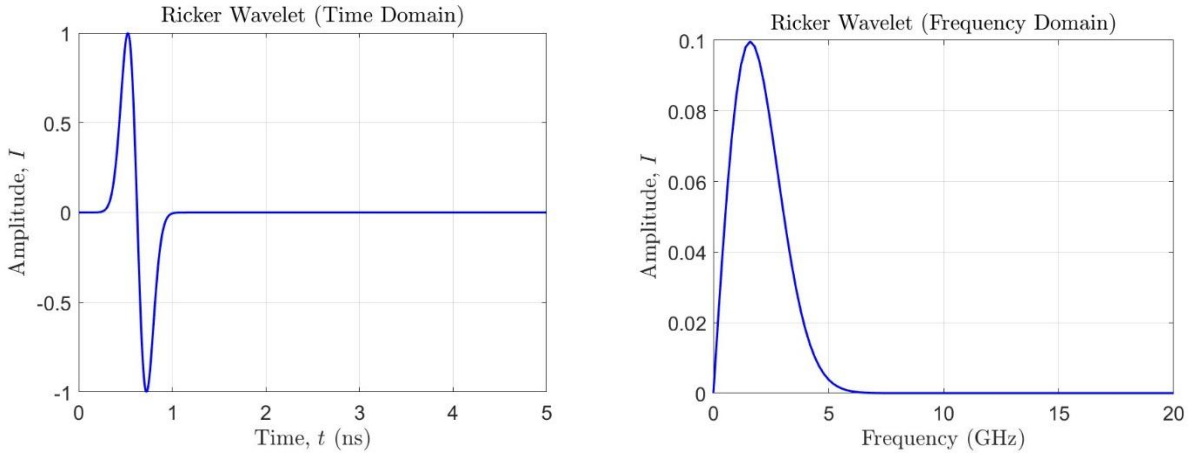


Fig. 3. Configuration of the concrete panel model.



(a) Ricker function in time domain. (b) Frequency spectrum of the ricker function.

Fig. 4. 1.6GHz ricker function as the input GPR signal.

A 1.6 GHz Ricker function is transmitted by the transmitting antenna Tx and measured by the receiving antenna Rx. An A-scan curve is the time-history of reflected Ricker function (GPR signal) when encountering an interface with dielectric contrast. Dielectric contrast is the ratio between the EM property of two dielectrics at their interface, which can be quantified by the reflection coefficient. When there is no dielectric contrast at an interface between two dielectrics, no reflection will be generated and measured by the receiving antenna Rx. In other words, GPR relies on the reflectivity of a subsurface target and cannot detect it if there is no reflection from the target.

In GPR B-scan, the location of Tx and Rx changes over time as the GPR system moves on the surface of a structure. The location of the receiving antenna Rx defines the traveling distance (also called the cross-range axis, r_x) from a reference origin each time when a B-scan takes place. For time-domain GPR systems, the reflected GPR signal is measured by Rx with an oscilloscope at a given location on the cross-range axis, in the form of a time history or a time series. By assuming a constant phase velocity v_p (propagation velocity) of the transmitted and the reflected GPR signals, the location of a subsurface reflection can be determined by

$$r = \frac{v_p t}{2} \quad (32)$$

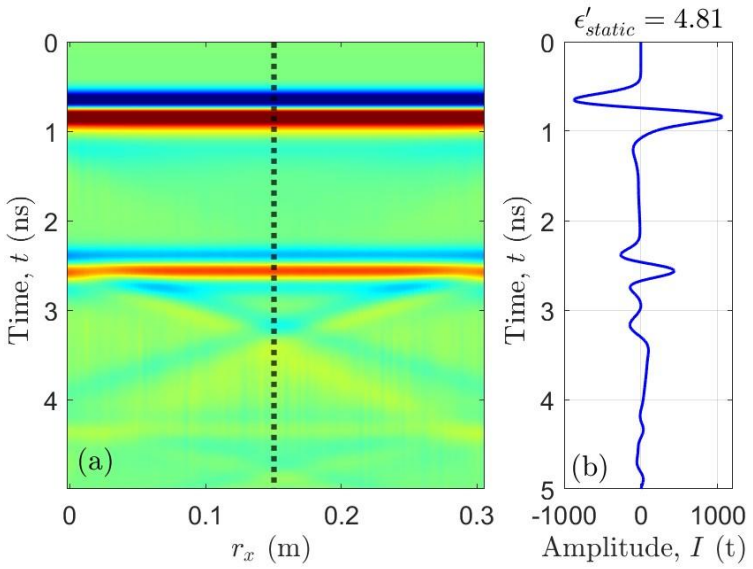
where r is the subsurface location of a subsurface reflection (m), v_p the phase velocity (m/s), and t the traveling time (sec) from Tx to Rx. Apparently, Eq. (32) is identical to Eq. (16) when $r = d$.

Assembly of various reflections in the space domain forms the depth axis, also known as the range axis, r. At a given location of r_x, reflected GPR signal measured by Rx forms the A-scan curve. By assembling multiple A-scan curves, a B-scan image is obtained. In our FDTD simulation, only two materials are considered: air and concrete as shown in Fig. 3. Therefore, two reflections are expected in our simulated A-scan curves and B-scan images.

4. Simulation Result

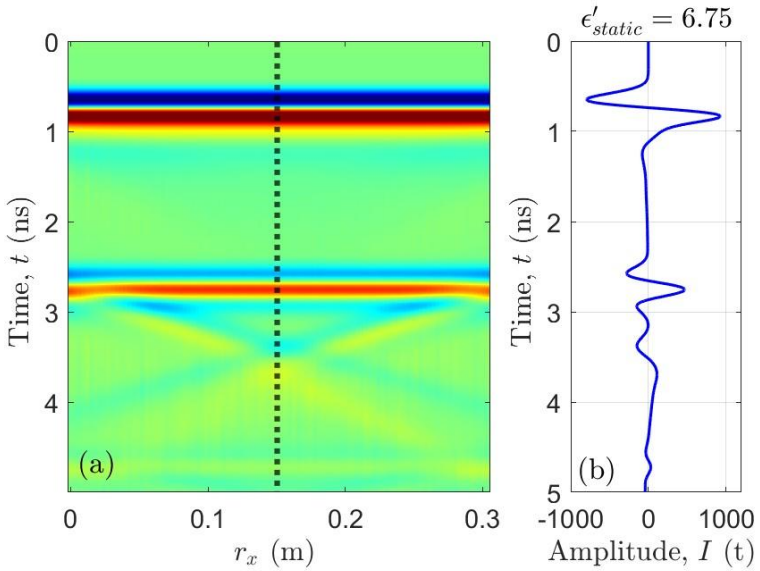
4.1. B-scan Images and A-scan Curves

Simulated B-scan images of concrete model CN1 and the A-scan curve at the center of concrete model CN1 are shown in Fig. 5. In Fig. 5, two reflections from the concrete model are seen: the surface/front reflection between the air-concrete interface (also known as the direct coupling signal) and the back reflection between the concrete-air interface. It is clear that the dielectric loss and electric conductivity attenuate the amplitude of GPR signal inside concrete. There are some corner reflections from the bottom of the concrete model in Fig. 5, which can be removed by using a time-windowing approach. Similarly, simulated B-scan images and A-scan curves of five other concrete models are shown in Figs. 6~10.



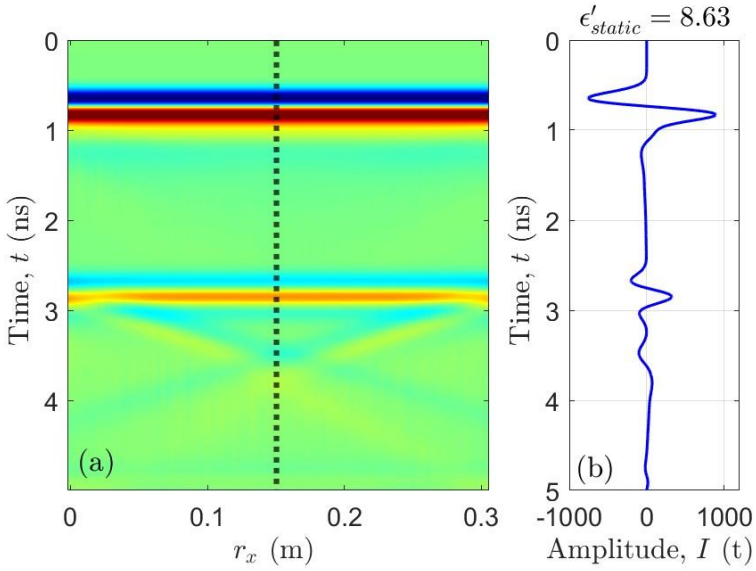
(a) B-scan image of model CN1. (b) A-scan curve of model CN1.

Fig. 5. Simulated GPR B-scan image and A-scan curve of concrete model CN1.



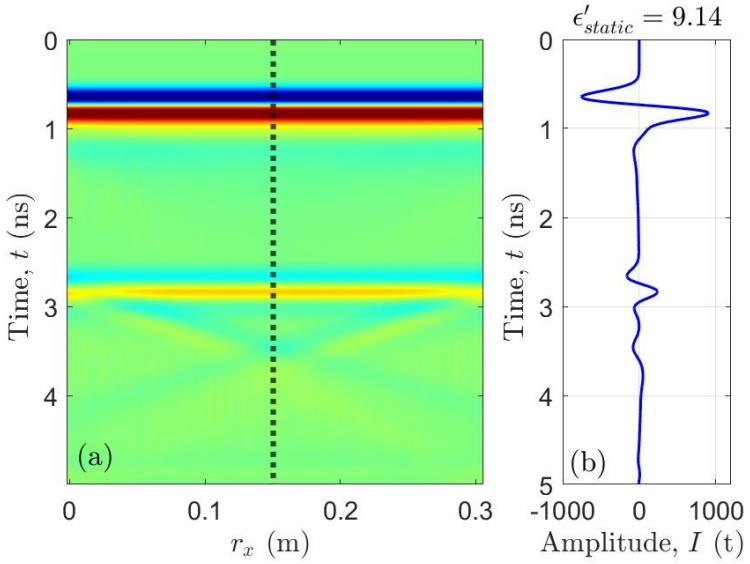
(a) B-scan image of model CN2. (b) A-scan curve of model CN2.

Fig. 6. Simulated GPR B-scan image and A-scan curve of concrete model CN2.



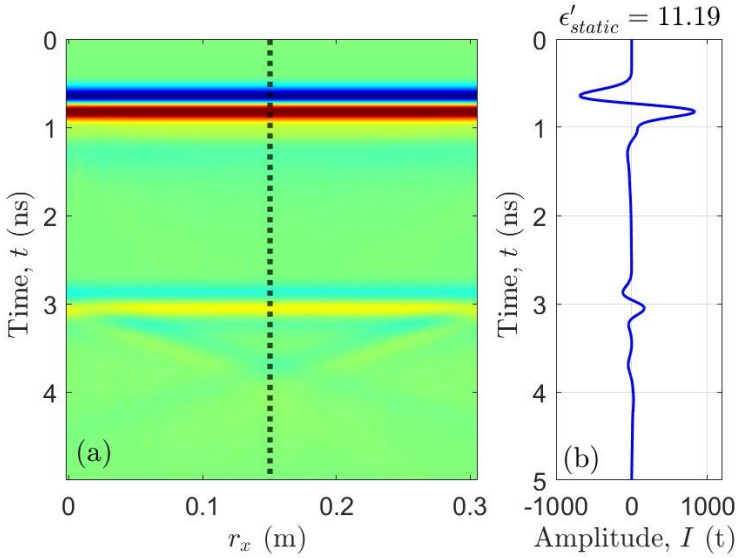
(a) B-scan image of model CN3. (b) A-scan curve of model CN3.

Fig. 7. Simulated GPR B-scan image and A-scan curve of concrete model CN3.



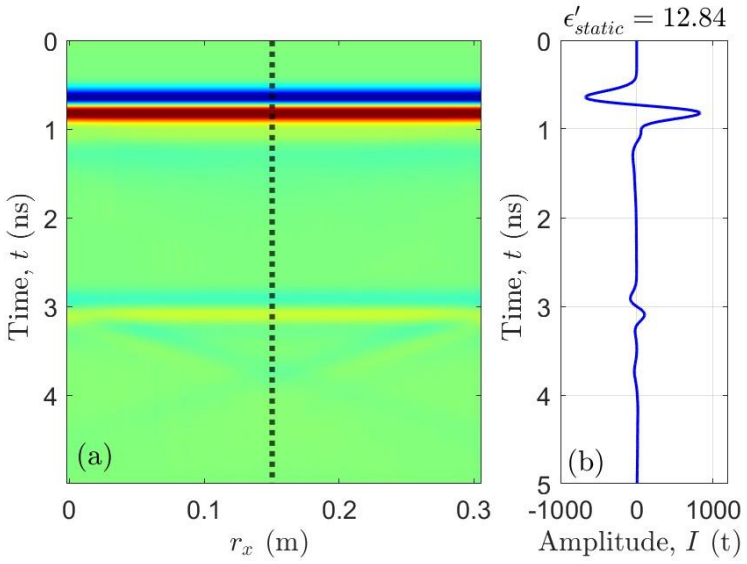
(a) B-scan image of model CN4. (b) A-scan curve of model CN4.

Fig. 8. Simulated GPR B-scan image and A-scan curve of concrete model CN4.



(a) B-scan image of model CN5. (b) A-scan curve of model CN5.

Fig. 9. Simulated GPR B-scan image and A-scan curve of concrete model CN5.



(a) B-scan image of model CN6. (b) A-scan curve of model CN6.

Fig. 10. Simulated GPR B-scan image and A-scan curve of concrete model CN6.

Fig. 11 compares the A-scan curves of six concrete models. Fig. 12 (a) shows the front reflection in A-scan curves of six concrete models, while Fig. 12 (b) shows the back reflection in A-scan curves of six concrete models. In Fig. 12 (a), we can see that the effect of moisture content leads

to the amplitude reduction of the front reflection GPR signal of concrete models, even though their dielectric constant $(\varepsilon_r')_D$ is increased from 4.6198 (0.2% moisture content) to 10.1914 (12% moisture content). This reduction is due to the increase of effective loss factor $\left(\varepsilon_{r,\text{eff}}''\right)_D$ from 0.19079 (0.2% moisture content) to 4.1634 (12% moisture content).

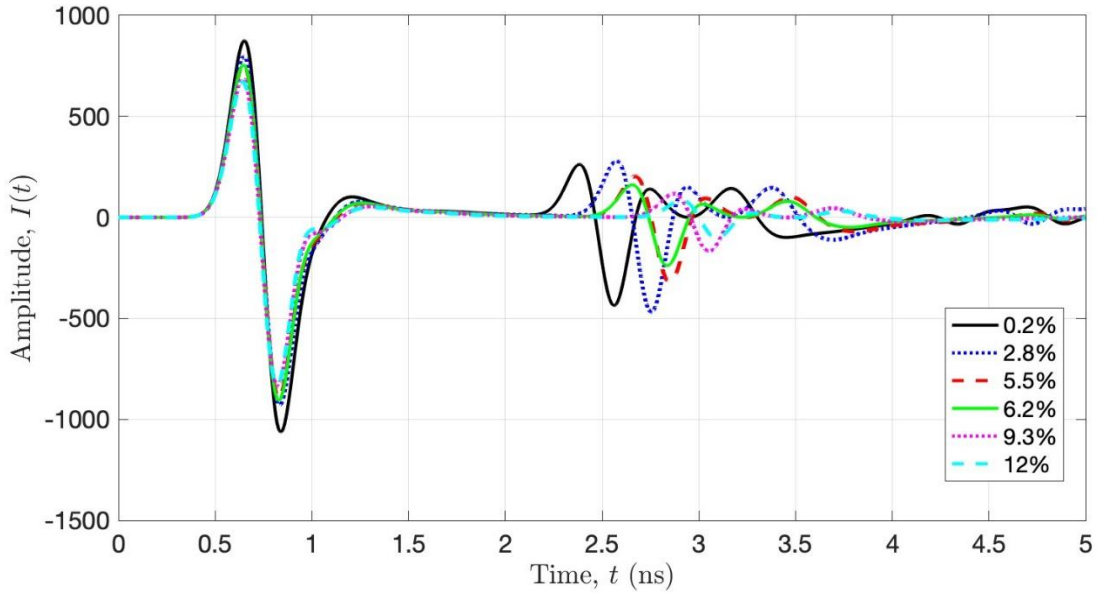
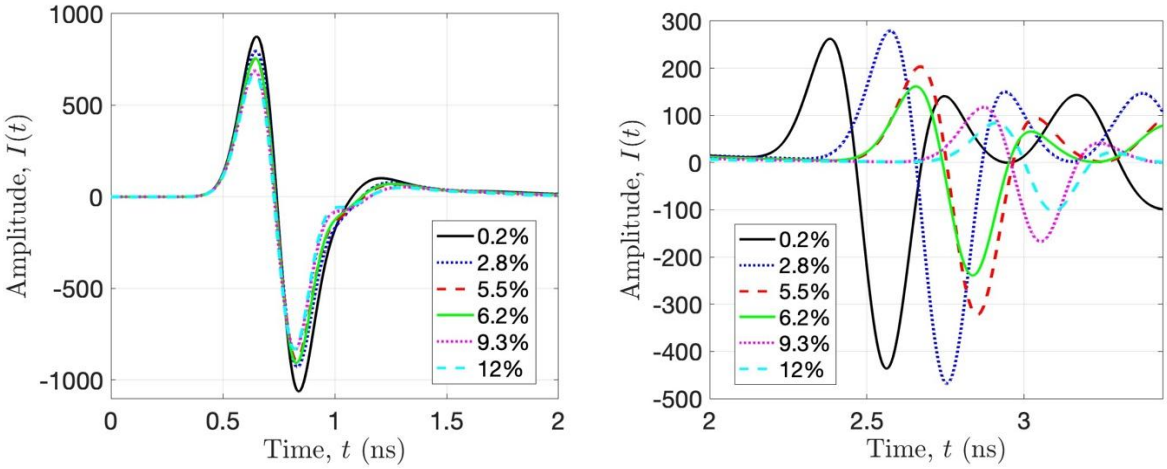


Fig. 11. Comparison of A-scan curves of six concrete models.



(a) Front reflection in A-scan curve. (b) Back reflection in A-scan curves.

Fig. 12. Comparison of front and back reflections in A-scan curves of six concrete models.

On the other hand, the effect of moisture content created even more drastic impact on the back reflection GPR signal. In Fig. 12 (b), both amplitude reduction and phase delay occur to the back reflection GPR signal. The delayed back reflection GPR signal in A-scan curves is due to the increase of dielectric constant of concrete, as explained by Eq. (13). Reduction of the back reflection amplitude is due to the increase of loss factor of concrete and the presence of electrical conductivity (due to the presence of moisture in concrete). Furthermore, we can also observe a phase change in all back reflection wave packets. This phase change has made the use of TDOA to determine ε_r' very challenging, if not impossible, especially in the presence of destructive interference in the waveform of back reflections. Phase change and destructive interference can shift the locations of the maximum and the minimum amplitudes of back reflections, resulting in unreliable TDOA values in the time domain.

4.2. Determination of Dielectric Constant $(\varepsilon_r')_A$ from A-scan Curves

To address the impact of phase change on the A-scan curves of concrete models with electrical conductivity, we avoided the direct use of TOA from the front and the back reflections in an A-scan curve. Instead, we used continuous wavelet transform (CWT) to determine the center of a wave packet. The time-domain A-scan curve of a concrete model is first converted to the wavelet domain by using CWT. The ricker wavelet was used in our CWT of A-scan curves due to its resemblance with the excitation source (which is also a ricker function), which is the main reason for us not to use other time-domain techniques such as short-time Fourier transform (STFT). Fig. 13 (a) provides the CWT of the A-scan curve from model CN1 as an example. Fig. 13 (b) provides the numbers of peak amplitudes in wavelet coefficients. In Fig. 13 (b), we can see that two TOA of two wave packets (front and back reflections). TDOA can be calculated from two TOA in Fig.

13 (c). For example, t_1=0.7406 ns and t_2=2.5356 ns from the CWT of A-scan curve of model CN1. TDOA for model CN1 is then t = 2.5356 – 0.7406 = 1.795 ns. With Eq. (15), we can use TDOA t to calculate the effective dielectric constant $(\varepsilon_r')_A$ from an A-scan curve. With Eq. (31), we can calculate $(\varepsilon_r')_D$. The difference $\Delta\varepsilon_r'$ is then determined by

$$\Delta\varepsilon_r' = (\varepsilon_r')_D - (\varepsilon_r')_A \quad (33)$$

This difference is due to the effect of dielectric lossness (including electrical conductivity) on the phase velocity of GPR signals since the back reflection is affected by the electrical conductivity of concrete. Table 2 compares the dielectric constant values from Debye's model and our A-scan curve approach.

Table 2. Comparison of dielectric constant from A-scan curves and Debye's model.

Model	Moisture content (%)	σ_{dc} (S/m)	$(\varepsilon_r')_A$	$(\varepsilon_r')_D$	$\Delta\varepsilon_r'$
CN1	0.2	6.06×10^{-4}	4.49472	4.6198	0.1226
CN2	2.8	2.03×10^{-3}	5.55491	5.5902	0.03529
CN3	5.5	5.15×10^{-3}	6.07834	6.7553	0.67696
CN4	6.2	6.7×10^{-3}	5.95492	7.1406	1.18568
CN5	9.3	23×10^{-3}	7.25684	8.8877	1.63086
CN6	12.0	20.6×10^{-3}	7.43869	10.1914	2.75271

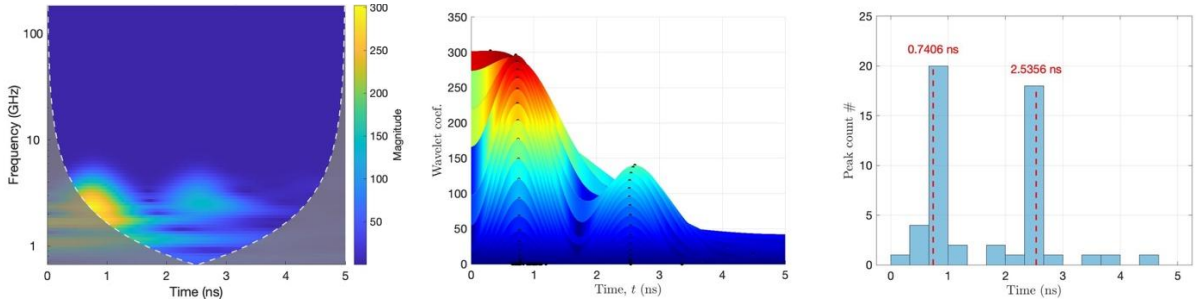
We found that this difference is closely related to the square root of electrical conductivity by

$$\Delta\varepsilon_r'(\sigma_{dc}) = 2.056 - 1.842\cos(231.7\sigma_{dc}) - 0.7999\sin(231.7\sigma_{dc}) \quad (34)$$

The performance of the $\Delta\varepsilon_r'(\sigma_{dc})$ model with data is shown in Fig. 14. In Fig. 14, the coefficient of determination (R^2) is 0.9994, demonstrating the accuracy of the model to capture the trend in the data. Consequently, the predicted dielectric constant $(\varepsilon_r')_A$ becomes

$$(\varepsilon_r')_A = \left(\frac{ct}{2d}\right)^2 + 2.056 - 1.842\cos(231.7\sigma_{dc}) - 0.7999\sin(231.7\sigma_{dc}) \quad (35)$$

In practice, σ_{dc} of concrete panel specimens can be experimentally measured. Fig. 15 illustrates the comparison between the ε_r' values from Debye's model and the A-scan curve model, demonstrating an excellent agreement. It should be pointed out that the parameters used in Debye's model to calculate $(\varepsilon_r')_D$ were determined from physical experiments [31,39,40], while $(\varepsilon_r')_A$ was determined from the GPR A-scan curve.



(a) CWT spectrum of A-scan. (b) Wavelet coefficients. (c) Histogram of wavelet coefficients.

Fig. 13. Wavelet coefficients and their histogram of A-scan curve – Model CN1.

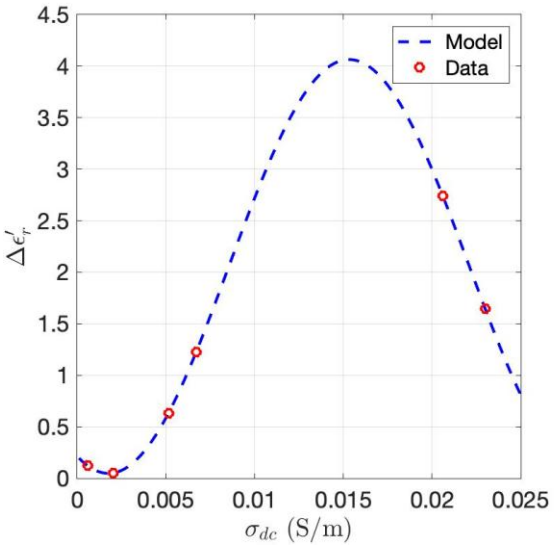


Fig. 14. Comparison of the $\Delta\varepsilon_r'(\sigma_{dc})$ model with data.

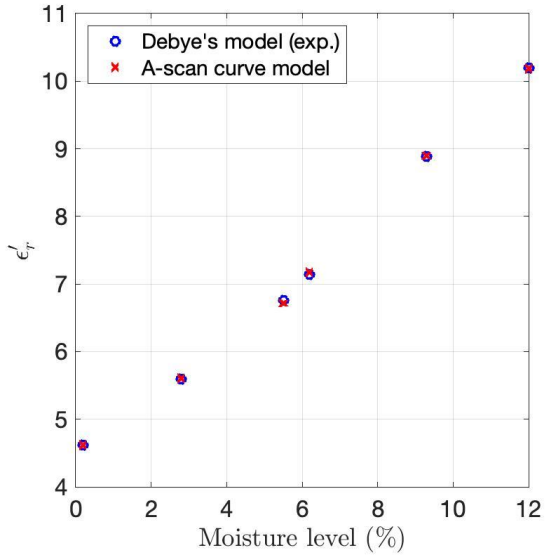


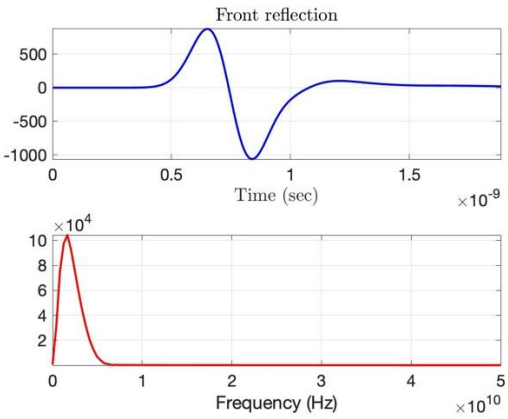
Fig. 15. Comparison of the ε'_r values from Debye's model and the A-scan curve model.

4.3. Determination of Effective Loss Factor $\left(\varepsilon''_{r,\text{eff}}\right)_A$ from A-scan Curves

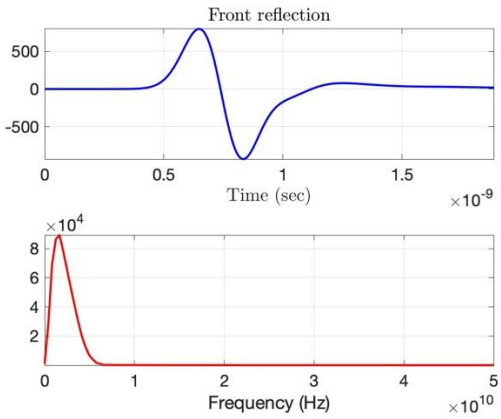
To determine effective loss factor $\left(\varepsilon''_{r,\text{eff}}\right)_A$ from A-scan curves using Eq. (26), we need to calculate $\ln\left(\frac{I_0}{I}\right)$. To avoid the confusion of using either positive or negative amplitude in A-scan curves, we used the spectral amplitude of the front and the back reflections of A-scan curves through converting time-domain A-scan curves to frequency-domain spectral curves with fast Fourier transform (FFT). CWT was not used in this purpose, in view of the issue with multiple spectral amplitudes at various scales in CWT spectrum. With $x = 2d$, Eq. (26) becomes

$$\left(\varepsilon''_{r,\text{eff}}\right)_A = \frac{4c\left(\varepsilon'_r\right)_A^{1.5}}{\omega d} M \ln\left(\frac{I_0}{I}\right) - 8\left(\varepsilon'_r\right)_A^2 \tag{36}$$

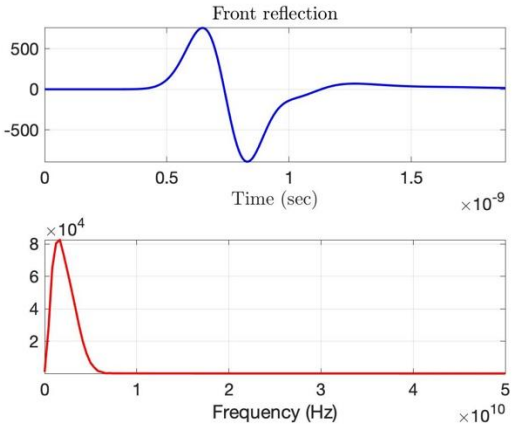
where $\left(\varepsilon'_r\right)_A$ is obtained from Eq.(35). Fig. 16 shows the frequency domain representation (spectral curve) of front reflections in A-scan curves, from which the value of input amplitude I_0 is calculated. Fig. 17 shows the frequency domain representation (spectral curve) of back reflections in A-scan curves, from which the value of attenuated amplitude I is calculated.



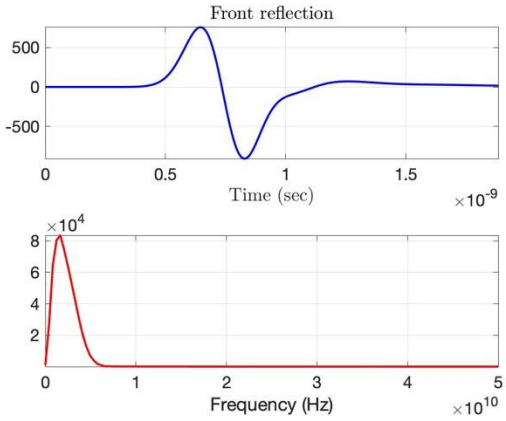
(a) Model CN1.



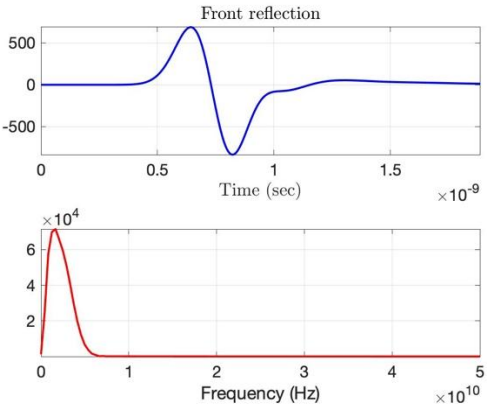
(b) Model CN2.



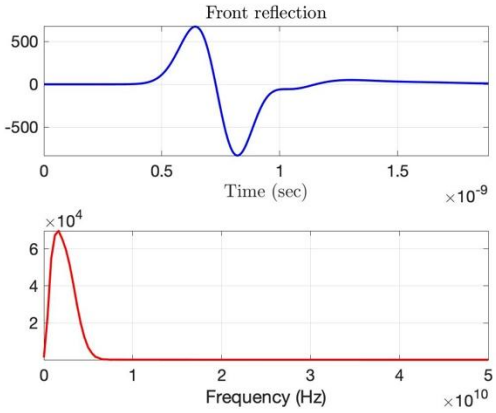
(c) Model CN3.



(d) Model CN4.

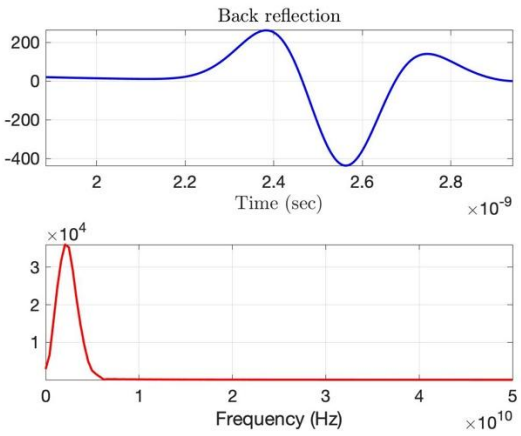


(e) Model CN5.

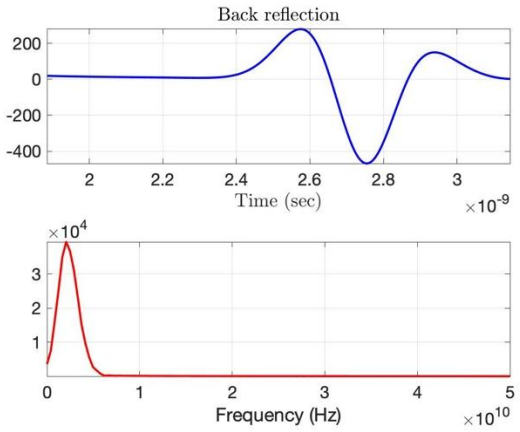


(f) Model CN6.

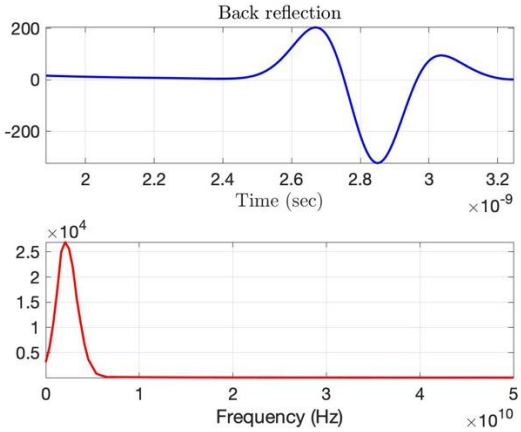
Fig. 16. Time domain and frequency domain representations of front reflections in A-scan curves of six concrete models.



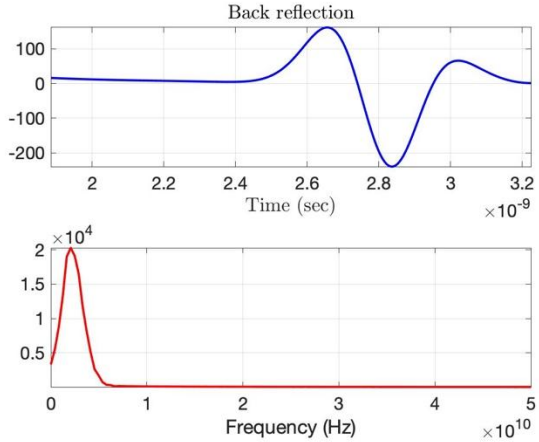
(a) Model CN1.



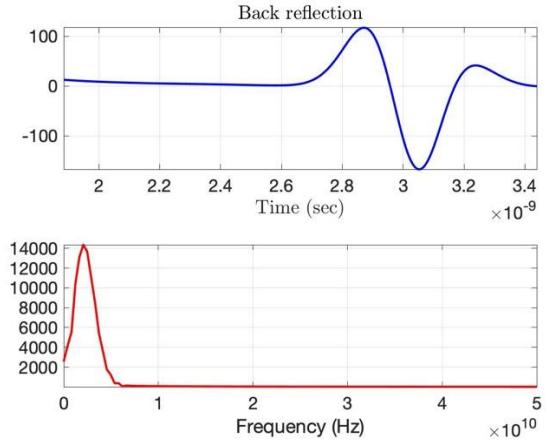
(b) Model CN2.



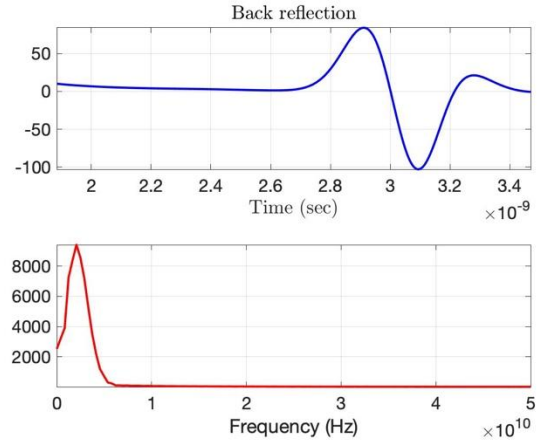
(c) Model CN3.



(d) Model CN4.



(e) Model CN5.



(f) Model CN6.

Fig. 17. Time domain and frequency domain representations of back reflections in A-scan curves of six concrete models.

Once we found the values of I_0 and I from the CWT spectrum of A-scan curves, we can calculate $\ln\left(\frac{I_0}{I}\right)$ to determine function M. From our analysis, we found that function M is closely correlated to dielectric constant by

$$M[(\varepsilon_r')_A] = 3.1765\sin(0.2351(\varepsilon_r')_A + 0.2243) + 0.8226\sin(1.6225(\varepsilon_r')_A - 1.6229) \quad (37)$$

Comparison of the calculated M value from probe measurement and $M[(\varepsilon_r')_A]$ is provided in Fig. 18. In Fig. 18, we can see that the $M[(\varepsilon_r')_A]$ model is in excellent agreement with calculated values, quantified by a R^2 value of 0.9998. With $M[(\varepsilon_r')_A]$, we compared $\left(\varepsilon''_{r,\text{eff}}\right)_A$ from Eq. (36) with reported experimental values from literatures in Fig. 19. In Fig. 19, our predicted $\left(\varepsilon''_{r,\text{eff}}\right)_A$ is also in excellent agreement with reported data with a R^2 value of 0.9996.

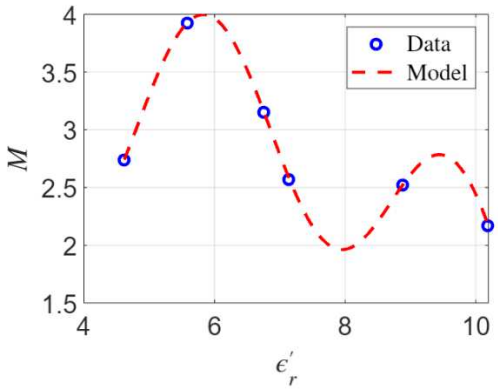


Fig. 18. Comparison between the $M(\varepsilon_r')$ model with data.

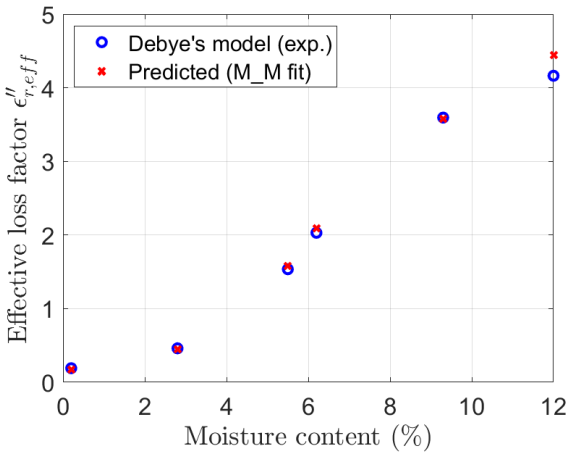


Fig. 19. Comparison of the $\varepsilon''_{r,\text{eff}}$ values from Debye's model and the A-scan curve model.

It is noteworthy to point out that, DC electrical conductivity σ_{dc} is needed in Eq. (35). σ_{dc} can be either experimentally measured or empirically estimated. Since our approach is based on the experimental data in Table 2, an empirical relation was developed between σ_{dc} and moisture content from Table 2.

$$\sigma_{DC} = 1.058 \times 10^{-4}(\psi - 0.2)^2 + 7.1708 \times 10^{-4}(\psi - 0.2) + 6.06 \times 10^{-4} \quad (38)$$

where ψ is the moisture content of concrete (in %). The performance of Eq. (38) is shown in Fig. 20 with a coefficient of determination of 0.848. In summary, our proposed procedure is illustrated in Fig. 21.

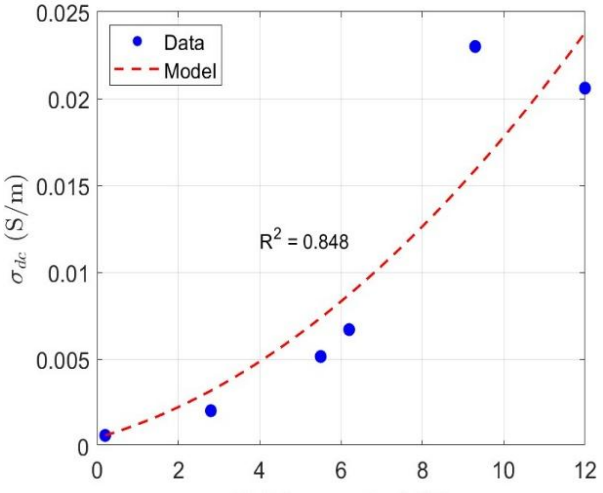


Fig. 20. Empirical relation between σ_{dc} and moisture content ψ.

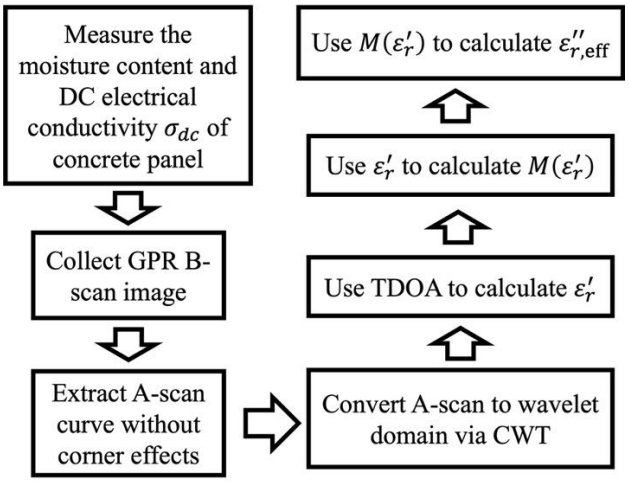
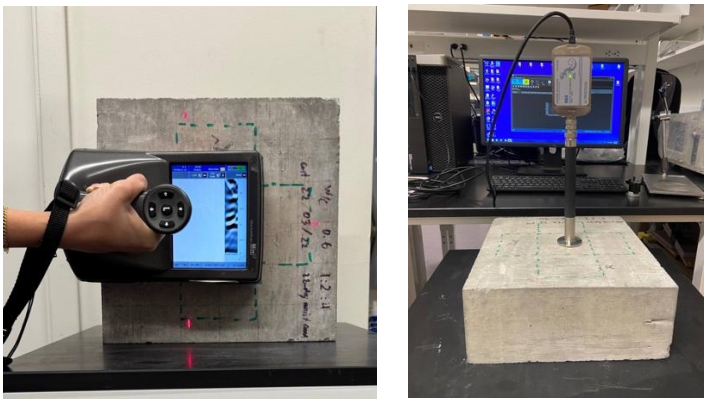


Fig. 21. Proposed procedure using GPR A-scan curves.

4.4. Application on a Laboratory Concrete Panel Specimen and Validation with a Coaxial Probe

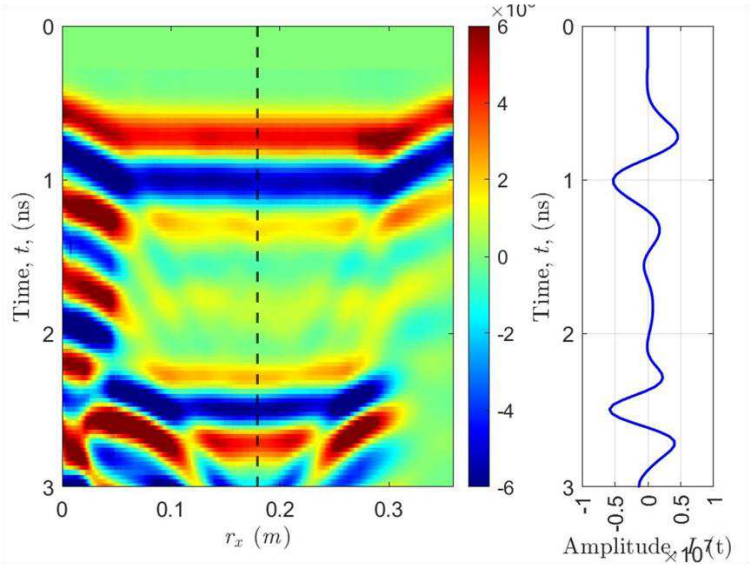
A laboratory concrete panel specimen (304.8×304.8×127 mm^3) was measured by a 1.6 GHz commercial GPR system (StructureScan by GSSI) to test our approach. The concrete panel was made of a 0.6 water-to-cement ratio and a mix ratio of 1:2:4 for cement:sand:gravel (by volume) and air dried for five years at a room temperature of 20° to 25° C with a current weight of 58.74

lbs. The moisture content (0.3416%) was experimentally measured by oven drying the specimen for two days to obtain the oven-dried weight (58.54 lbs). Fig. 22 illustrates the GPR B-scan configuration of the specimen. Obtained B-scan image and the mid-section A-scan curve are shown in Fig. 23.



(a) (b)

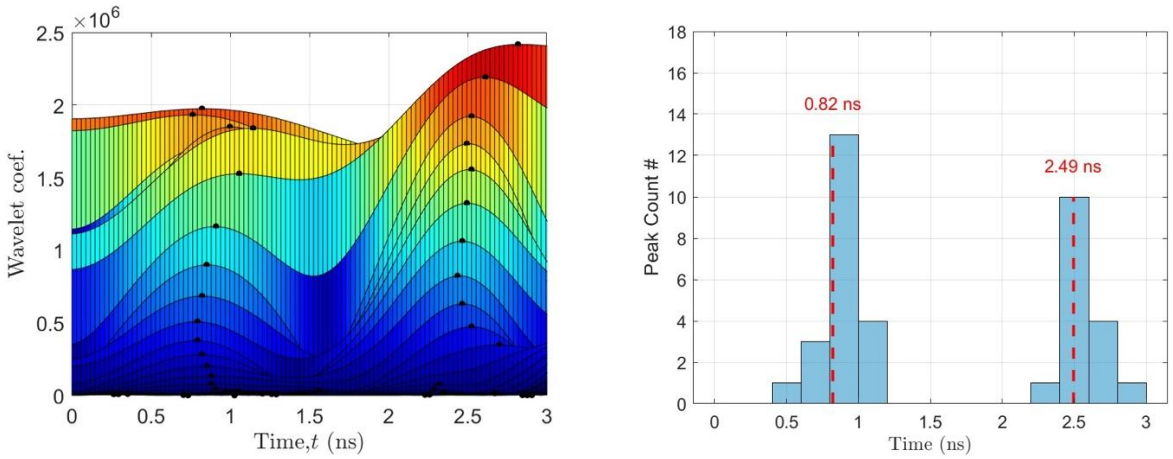
Fig. 22. GPR B-scan and probe measurement of the concrete panel specimen.



(a) (b)

Fig. 23. GPR B-scan image and mid-section A-scan curve of the concrete specimen.

The CWT of the A-scan curve and the histogram of peak amplitudes are shown in Fig. 24 (a) and (b), respectively. From Fig. 24 (b), the center of the first wave packet is 0.82ns and the center of the second wave packet to be 2.49ns, indicating that the TDOA (t) is 1.67ns. From Eq. (34), the predicted dielectric constant $(\varepsilon_r')_A$ was calculated to be 3.9984. Converting the time-domain first wave packet and the second wave packet through FFT to the frequency domain led to the result in Fig. 25. From Fig. 25 (c), the spectral amplitude I_0 is 2,136,960,000 and I to be 58,884,200. From Eq. (36), the value of function M was calculated to be 2.1046. From Eq. (35), we computed the value of effective loss factor to be 0.1882.



(a) CWT of A-scan curve. (b) Histogram of peak amplitudes.

Fig. 24. GPR B-scan image and mid-section A-scan curve of the concrete specimen.

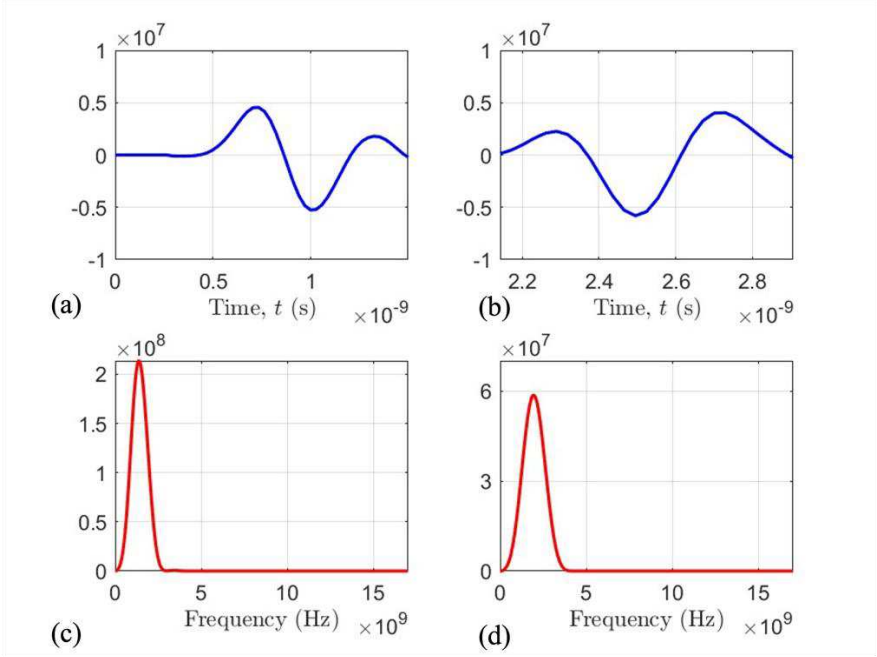
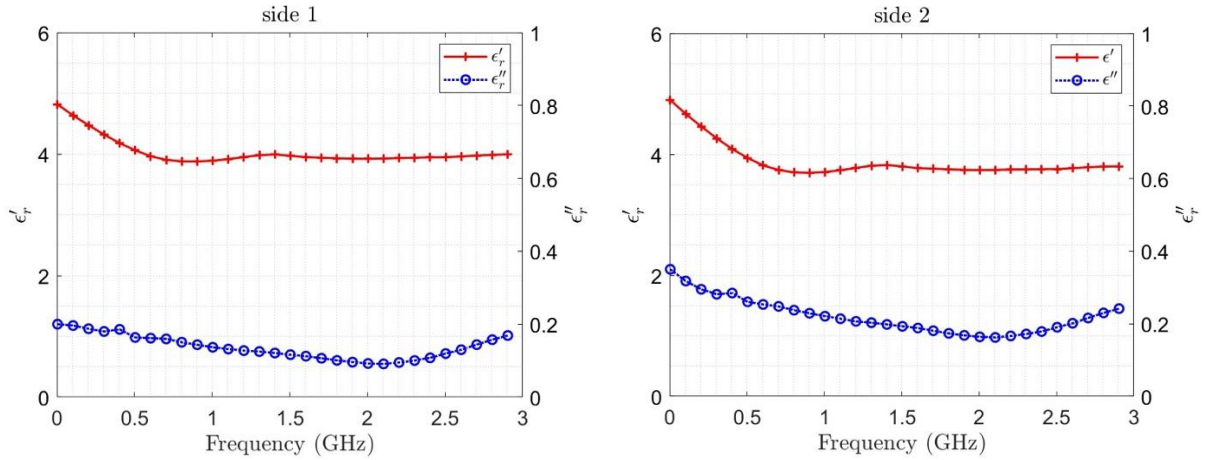


Fig. 25. The first wave packet and the second wave packet and their FFT spectral curves.



(a) (b)

Fig. 26. Measured dielectric constant and loss factor on two sides of the concrete panel.

To validate our predicted dielectric constant and effective loss factor, we used a coaxial probe (DAK 12, 4MHz ~ 3GHz) to directly measure the dielectric constant and loss factor of the concrete panel. To account for the heterogeneity of concrete, we measured two sides of the panel to obtain average values. Fig. 26 shows the measured dielectric constant and loss factor values of two sides

of the concrete panel. The average values at 1.6GHz were 3.9474 for dielectric constant and 0.1123 for loss factor. Table 3 compares our predicted values with the values measured by the coaxial probe. Theoretical values by Debye's model in Eqs. (28) and (31) are also provided in Table 3.

Table 3. Comparison of proposed approach with Debye's model and probe measurement at 1.6GHz.

	Our approach	**Debye's model**	**Difference (%)**	**Probe measurement**	**Difference (%)**
$\boldsymbol{\varepsilon'_{r,\mathrm{eff}}}$	3.9984	4.6198	-13.45	3.9474	1.29
$\boldsymbol{\varepsilon''_{r,\mathrm{eff}}}$	0.1882	0.1908	-1.36	0.1123	67.58

In Table 3, our approach predicts a dielectric constant value very close to probe measurement with a 1.29% difference and a loss factor value very close to Debye's model value with a -1.36% difference. The loss factor prediction shows a large difference with probe measurement. This difference is attributed to i) non-uniform moisture distribution inside concrete, and ii) limited penetration of the probe. Our predicted loss factor is close to the theoretical loss factor calculated by Debye's model with a -1.36% difference. Should we use Debye's model (upper bound) and probe measurement (lower bound) as two limits, our predicted values within these two bounds.

5. Conclusion

In this paper, we proposed an approach to solve the long-standing problem of loss factor estimation in GPR data. Our approach on predicting dielectric constant and loss factor of concrete panels utilizes the GPR A-scan curve of concrete panels. The used A-scan curve, including the front reflection (direct coupling) wave packet and the back reflection wave packet, at the mid-section of concrete panels is used to avoid the detrimental corner effect (destructive interference) in wave scattering. Continuous wavelet transform (CWT) is applied to the A-scan curve to determine the

TDOA (time difference of arrival) between the front reflection and the back reflection. Attenuation of GPR signals from the front reflection to the back reflection is calculated in the frequency domain, rather than using the time domain amplitude in conventional approaches. A modification function M is proposed to account for the combined effect of material composition, specimen geometry, wave scattering and interference. Numerical simulation using the finite difference time domain (FDTD) method is conducted by using material properties reported in the literature to generate synthetic A-scan curves. Our predicted dielectric constant and loss factor values are validated by experimental GPR data on a laboratory concrete panel specimen. From our result, it is found that our predicted dielectric constant and loss factor are lower than theoretical values by Debye's model and higher than probe measurement. Since GPR is a portable and commercially mature technique in civil engineering, our approach can better predict the dielectric property of concrete in a practical configuration. Furthermore, the knowledge of dielectric constant and loss factor of concrete can assist the image processing of concrete structures for better concrete crack detection and steel rebar corrosion in the future.

Acknowledgement

We would like to thank the U.S. Department of Transportation (DOT) for partially supporting this research through a UTC (University Transportation Center) TIDC (Transportation Infrastructure Durability Center) (led by H. Dagher from UMaine) Project 1.4 "Electromagnetic Detection and Identification of Concrete Cracking in Highway Bridges" to UMass Lowell (PI: Tzuyang Yu).

Disclaimer

The contents of the research presented in this paper reflect the views of the researchers, who are responsible for the facts and the accuracy of the information presented. The findings presented in

this paper are disseminated in the interest of information exchange. The research presented in this paper is funded, partially or entirely, by a grant from the U.S. Department of Transportation's University Transportation Centers Program. However, the U.S. Government assumes no liability for the contents or use thereof.

References

[1] B.I. L AI-Qadi, O.A. Hazim, W. Su, S.M. Riad, Dielectric properties of Portland cement concrete at low radio frequencies, ASCE J Mater Civil Eng 7:3 (1995). https:doi.org/10.1061/(ASCE)0899-1561(1995)7:3(192).

[2] M. Jamil, M.K. Hassan, H.M.A. Al-Mattarneh, M.F.M. Zain, Concrete dielectric properties investigation using microwave nondestructive techniques, Materials and Structures/Materiaux et Constructions 46 (2013) 77–87. https://doi.org/10.1617/s11527-012-9886-2.

[3] A. Robert, Dielectric permittivity of concrete between 50 MHz and 1 GHz and GPR measurements for building materials evaluation, J Appl Geophys 40:1-3 (1998). https://doi.org/10.1016/S0926-9851(98)00009-3.

[4] T.T. Dinh, S. Hegler, M. Liebscher, I. Navarro de Sosa, H. Li, D. Plettemeier, W.G. Drossel, V. Mechtcherine, Dielectric material characterization of concrete in GHz range in dependence on pore volume and water content, Constr Build Mater 311 (2021). https://doi.org/10.1016/j.conbuildmat.2021.125234.

[5] S. Soldatov, M. Umminger, A. Heinzel, G. Link, B. Lepers, J. Jelonnek, Dielectric characterization of concrete at high temperatures, Cem Concr Compos 73 (2016) 54–61. https://doi.org/10.1016/j.cemconcomp.2016.01.006.

[6] H. Xu, B. Li, S. Xu, H. Feng, The measurement of dielectric constant of the concrete using single-frequency CW radar, in: Proceedings - The 1st International Conference on Intelligent Networks and Intelligent Systems, ICINIS 2008 (2008) 588–591. https://doi.org/10.1109/ICINIS.2008.139.

[7] Y. Shen, C.L. Law, W. Doui, Ultra-Wideband Measurement of the Dielectric Constant and Loss Tangent of Concrete Slabs, In: Proc. 2008 China-Japan Joint Microwave Conf. (2009). https:10.1109/CJMW.2008.4772488.

[8] G. Klysz, J.P. Balayssac, X. Ferrières, Evaluation of dielectric properties of concrete by a numerical FDTD model of a GPR coupled antenna-Parametric study, NDT and E International 41 (2008) 621–631. https://doi.org/10.1016/j.ndteint.2008.03.011.

[9] S.S. Zhekov, O. Franek, G.F. Pedersen, Dielectric Properties of Common Building Materials for Ultrawideband Propagation Studies [Measurements Corner], IEEE Antennas Propag Mag 62 (2020) 72–81. https://doi.org/10.1109/MAP.2019.2955680.

[10] O. Büyüköztürk, T.Y. Yu, J.A. Ortega, A methodology for determining complex permittivity of construction materials based on transmission-only coherent, wide-bandwidth free-space measurements, Cem Concr Compos 28 (2006) 349–359. https://doi.org/10.1016/j.cemconcomp.2006.02.004.

[11] S. Stavrou, S.R. Saunders, Review of constitutive parameters of building materials, n.d.

[12] P.T. wai Wong, W.W. lok Lai, Characterization of Complex Dielectric Permittivity of Concrete by GPR Numerical Simulation and Spectral Analysis, J Nondestr Eval 41 (2022). https://doi.org/10.1007/s10921-021-00836-z.

[13] W. Chen, P. Shen, Z. Shui, Determination of water content in fresh concrete mix based on relative dielectric constant measurement, Constr Build Mater 34 (2012) 306–312. https://doi.org/10.1016/j.conbuildmat.2012.02.073.

[14] W.L. Lai, S.C. Kou, W.F. Tsang, C.S. Poon, Characterization of concrete properties from dielectric properties using ground penetrating radar, Cem Concr Res 39 (2009) 687–695. https://doi.org/10.1016/j.cemconres.2009.05.004.

[15] R. He, T. Nantung, J. Olek, N. Lu, Field study of the dielectric constant of concrete: A parameter less sensitive to environmental variations than electrical resistivity, Journal of Building Engineering 74 (2023). https://doi.org/10.1016/j.jobe.2023.106938.

[16] R. He, N. (Luna) Lu, Unveiling the dielectric property change of concrete during hardening process by ground penetrating radar with the antenna frequency of 1.6 GHz and 2.6 GHz, Cem Concr Compos 144 (2023). https://doi.org/10.1016/j.cemconcomp.2023.105279.

[17] Z. Hou, H. Liu, J. Cheng, Q. Zhang, Z. Tong, Permittivity Measurement in Multi-Phase Heterogeneous Concrete Using Evidential Regression Deep Network and High-Frequency Electromagnetic Waves, Materials 18 (2025) 3766. https://doi.org/10.3390/ma18163766.

[18] G. Klysz, J.P. Balayssac, S. Laurens, Spectral analysis of radar surface waves for non-destructive evaluation of cover concrete, NDT and E International 37 (2004) 221–227. https://doi.org/10.1016/j.ndteint.2003.09.006.

[19] G. Klysz, X. Ferrieres, J.P. Balayssac, S. Laurens, Simulation of direct wave propagation by numerical FDTD for a GPR coupled antenna, NDT and E International 39 (2006) 338–347. https://doi.org/10.1016/j.ndteint.2005.10.001.

[20] A. Alzeyadi, T. Yu, Subsurface characterization of moisture content and water-to-cement ratio of concrete specimens using remote synthetic aperture radar imaging, (2020). https://doi.org/10.1117/1.JRS.14.

[21] Arthur R. von Hippel, Dielectrics and Waves, MIT Press, Cambridge, MA, 1954.

[22] Wait, James R, Electromagnetic wave theory, Harper & Row, New York, NY, 1985.

[23] Dudley H. Towne, Wave Phenomena, Addison-Wesley Publishing Company, Toronto, Canada, 1967.

[24] Allen Taflove, Susan C Hagness, Computational Electrodynamics: The Finite-Difference Time-Domain Method, Third Edition, 3rd ed., Artech House Publishers, Norwood, MA, 2005.

[25] Tzuyan Yu, Burak Boyaci, H.Flix Wu, Simulated Transient Electromagnetic Response for the Inspection of GFRP-Wrapped Concrete Cylinders Using Radar NDE, Research in Nondestructive Evaluation (2013) 125-153. https://doi.org/10.1080/09349847.2012.713162

[26] Stephen Gedney, Introduction to the Finite-Difference Time-Domain (FDTD) Method for Electromagnetics (Synthesis Lectures on Computational Electromagnetics), 1st ed., Springer, 2011.

[27] Shahid Ahmed, Electromagnetic Pulse Simulations Using Finite-Difference Time-Domain Method, Wiley, 2021.

[28] Karl S.Kunz, Raymond J.Luebber, The Finite Difference Time Domain Method for Electromagnetics, 1st ed., CRC Press, 2018.

[29] Shumin Wang, Fernando L. Teixeira, Robert Lee, Advances in Time-Domain Computational Electromagnetics: Beyond Conventional Finite Difference Methods, VDM Verlag Dr. Müller, 2010.

[30] gprMax: Open source electromagnetic wave simulator, (2026). https://www.gprmax.com

[31] L. Sandrolini, U. Reggiani, A. Ogunsola, Modelling the electrical properties of concrete for shielding effectiveness prediction, J Phys D Appl Phys 40 (2007) 5366–5372. https://doi.org/10.1088/0022-3727/40/17/053.

[32] M.N. Soutsos, J.H. Bungey, S.G. Millard, M.R. Shaw, A. Patterson, Dielectric properties of concrete and their influence on radar testing, NDT&E Intl 34:6 (2001) 419-425. https://doi.org/10.1016/S0963-8695(01)00009-3.

[33] A. Shaari, S.G. Millard, J.H. Bungey, Modelling the propagation of a radar signal through concrete as a low-pass filter, NDT and E International 37 (2004) 237–242. https://doi.org/10.1016/j.ndteint.2003.09.009.

[34] J.-P. Berenger, A Perfectly Matched Layer for the Absorption of Electromagnetic Waves, J Comp Phys 114:2 (1994) 185-200. https://doi.org/10.1006/jcph.1994.1159.

[35] F.L. Teixeira, W.C. Chew, General Closed-Form PML Constitutive Tensors to Match Arbitrary Bianisotropic and Dispersive Linear Media, IEEE Microwave Guided Wave Letters 8:6 (1998) 223-225. https://doi.org/10.1109/75.678571.

[36] V. Kalvin, Analysis of perfectly matched layer operators for acoustic scattering on manifolds with quasicylindrical ends, Journal Des Mathematiques Pures et Appliquees 100 (2013) 204–219. https://doi.org/10.1016/j.matpur.2012.12.001.

[37] V. Kalvin, Limiting absorption principle and perfectly matched layer method for dirichlet laplacians in quasi-cylindrical domains, SIAM Journal on Mathematical Analysis 44 (2012) 355–382. https://doi.org/10.1137/110834287.

[38] K. Friedrichs, H Lewyt, R. Courant. On the Partial Difference Equations of Mathematical Physics, IBM Journal (1967) 215-234. https://10.1147/rd.112.0215.

[39] G. Klysz, J.P. Balayssac, Determination of volumetric water content of concrete using ground-penetrating radar, Cem Concr Res 37 (2007) 1164–1171. https://doi.org/10.1016/j.cemconres.2007.04.010.

[40] W.L. Lai, T. Kind, H. Wiggenhauser, A study of concrete hydration and dielectric relaxation mechanism using ground penetrating radar and short-time Fourier transform, EURASIP J Adv Signal Process 2010 (2010). https://doi.org/10.1155/2010/317216.